

LETTER TO THE EDITOR

# Extreme intra-hour variability of the radio source J1402+5347 discovered with Apertif

T.A. Oosterloo<sup>1,2</sup>, H.K. Vedantham<sup>1,2</sup>, A.M. Kutkin<sup>1,3</sup>, E. A. K. Adams<sup>1,2</sup>, B. Adebahr<sup>4</sup>, A.H.W.M. Coolen<sup>1</sup>,  
S. Damstra<sup>1</sup>, W.J.G. de Blok<sup>1,2,5</sup>, H. Dénes<sup>1</sup>, K.M. Hess<sup>1,2</sup>, B. Hut<sup>1</sup>, G.M. Loose<sup>1</sup>, D.M. Lucero<sup>2,6</sup>,  
Y. Maan<sup>1,7</sup>, R. Morganti<sup>1,2</sup>, V.A. Moss<sup>1,8,9</sup>, H. Mulder<sup>1</sup>, M.J. Norden<sup>1</sup>, A.R. Offringa<sup>1</sup>, L.C. Oostrum<sup>1,7</sup>,  
E. Orrù<sup>1</sup>, M. Ruiter<sup>1</sup>, R. Schulz<sup>1</sup>, R.H. van den Brink<sup>10</sup>, J.M. van der Hulst<sup>2</sup>, J. van Leeuwen<sup>1,7</sup>,  
N.J. Vermaas<sup>1</sup>, D. Vohl<sup>1</sup>, S.J. Wijnholds<sup>1</sup>, J. Ziemke<sup>1,11</sup>

<sup>1</sup>ASTRON, the Netherlands Institute for Radio Astronomy, Oude Hoogeveensedijk 4, 7991 PD Dwingeloo, The Netherlands

<sup>2</sup>Kapteyn Astronomical Institute, University of Groningen, Postbus 800, 9700 AV Groningen, The Netherlands

<sup>3</sup>Astro Space Center of Lebedev Physical Institute, Profsoyuznaya Str. 84/32, 117997 Moscow, Russia

<sup>4</sup>Astronomisches Institut der Ruhr-Universität Bochum (AIRUB), Universitätsstrasse 150, 44780 Bochum, Germany

<sup>5</sup>Department of Astronomy, University of Cape Town, Private Bag X3, Rondebosch 7701, South Africa

<sup>6</sup>Department of Physics, Virginia Polytechnic Institute and State University, 50 West Campus Drive, Blacksburg, VA 24061, USA

<sup>7</sup>Anton Pannekoek Institute, University of Amsterdam, Postbus 94249, 1090 GE Amsterdam, The Netherlands

<sup>8</sup>CSIRO Astronomy and Space Science, Australia Telescope National Facility, PO Box 76, Epping NSW 1710, Australia

<sup>9</sup>Sydney Institute for Astronomy, School of Physics, University of Sydney, Sydney NSW 2006, Australia

<sup>10</sup>Tricas Industrial Design & Engineering, Hanzelaan 95b, 8017 JE Zwolle, The Netherlands

<sup>11</sup>Center for Information Technology, University of Groningen, Postbus 11044, 9700 CA Groningen, the Netherlands

## ABSTRACT

Propagation of the radio waves from distant compact radio sources through turbulent interstellar plasma in our Galaxy leads to twinkling of these sources, a phenomenon called interstellar scintillation. Such scintillations are a unique probe of the micro-arcsecond structure of radio sources as well as of the sub-AU-scale structure of the Galactic interstellar medium. Weak scintillations (i.e. intensity modulation of a few per cent) on timescales of a few days or longer are commonly seen at centimetre wavelengths and are thought to result from the line-of-sight integrated turbulence in the Milky Way's interstellar plasma. So far, only three sources were known that show more extreme variations, with modulations at the level of tens of per cent on timescales less than an hour. This requires propagation through nearby ( $d \lesssim 10$  pc) anomalously dense ( $n_e \sim 10^2$  cm<sup>-3</sup>) plasma clouds. Here we report the discovery with Apertif of a source (J1402+5347) showing extreme ( $\sim 50\%$ ) and rapid variations on a timescale of just 6.5 minutes in the decimetre band (1.4 GHz). The spatial scintillation pattern is highly anisotropic with a semi-minor axis of about 20,000 km. Canonical theory of refractive scintillation constrains the scattering plasma to be within the Oort cloud. The sight-line to J1402+5347 however passes unusually close to the B3 star Alkaid ( $\eta$  UMa) at a distance of 32 pc. If the scintillations are associated with Alkaid, then the angular size of J1402+5347 along the minor-axis of the scintels must be smaller than  $\approx 10$   $\mu$ s yielding an apparent brightness temperature for an isotropic source of  $\gtrsim 10^{14}$  K.

**Key words.** scattering – ISM: clouds – quasars: individual: J1402+5347

## 1. Introduction

Intra-hour variability (IHV) refers to quasi-random intensity modulation similar to canonical interstellar scintillation, but on vastly shorter timescales. It is an extreme manifestation of radio-wave propagation through turbulent plasma, but the nature of the plasma clouds causing the fast variability has remained unclear so far. It is generally thought to be caused by nearby ( $d \sim 10$  pc) turbulent plasma (Bignall et al. 2007; de Bruyn & Macquart 2015). Because the scattering strength of plasma is weaker if the plasma clouds are at small distances, the plasma densities inferred from IHV observations are orders of magnitude larger than that in the ambient ionised interstellar gas. The formation and survival of such over-pressured clouds is at the heart of the mystery. No multi-wavelength counterparts to the plasma have yet been found.

A recent development is the statistical association of three known IHVs with nearby hot stars (Walker et al. 2017). These

authors suggest that the scattering is caused by the ionised sheath of tiny self-gravitating molecular clumps similar to the cometary knots seen in, for example, the Helix nebula. If true, this would be extremely interesting as these clouds would constitute a new population of objects within the interstellar medium. Alternatively, Pen & King (2012) and Pen & Levin (2014) have refined the model of Goldreich & Sridhar (2006), which suggests that the extreme scattering phenomena are caused by thin plasma sheets (which have a basis in MHD theory) oriented along the sight-line. The implication here being that there is nothing inherently unusual about the intervening plasma save a fortuitous orientation.

Only very few IHVs are known. More such objects need to be discovered to better understand their statistical properties and for more secure empirical associations. More cases with extreme properties need to be studied to test the limits of proposed theories. The recent spate of wide-field survey radio telescopes oper-

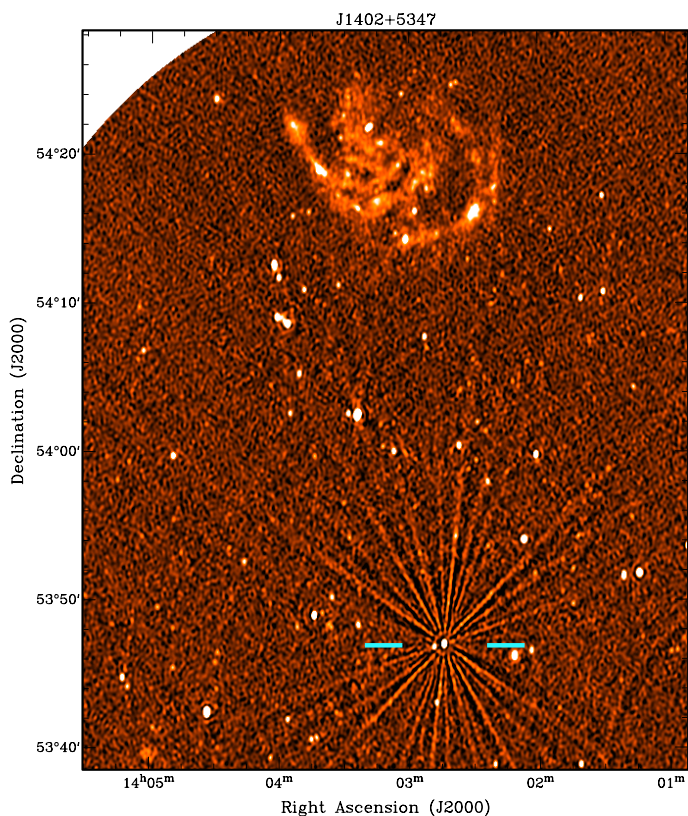


**Fig. 1.** Discovery image of J1402+5347 (marked by the blue lines) made from the observation on April 9, 2019. The galaxy to the north is the nearby spiral galaxy M101. The prominent radial spikes centred on J1402+5347 led to its identification as a highly variable source.

ating in the GHz band, such as ASKAP in Australia and Apertif on the Westerbork Synthesis Radio Telescope (WSRT), are in an excellent position to provide larger samples. Here we report on the first IHV discovered by the recently started survey with the Apertif phased-array frontends on the WSRT.

## 2. Discovery and follow-up

We serendipitously discovered large and rapid scintillations in the radio source J1402+5347 (RA<sub>J2000</sub> 14<sup>h</sup> 02<sup>m</sup> 43<sup>s</sup>.6, Dec<sub>J2000</sub> 53°47'11'') with the Apertif phased-array feed system on the WSRT in commissioning data taken on April 9, 2019. Due to the east-west orientation of the WSRT, highly variable sources show prominent artefacts in the form of radial spikes in long-exposure images which makes them easy to identify (Fig. 1). The light-curve extracted for the source (Fig. 2; details in Appendix A) shows large flux-density variations which are about 38% of the mean value. Archival WSRT observations from 2013 of the same field at the same frequency showed no significant variability in J1402+5347. In optical images no counterpart is visible to J1402+5347, but in images produced by the WISE satellite (Cutri et al. 2012) an object is present at the location of J1402+5347. The lack of an optical counterpart, together with the colours of this object in the WISE data, suggests that the background object is a dust-obscured AGN at fairly high redshift ( $z \gtrsim 1$ ; Jarrett et al. 2017).

Follow-up observations taken in May also showed large variability, at the level of about 30%. Further observations in June and July 2019 showed lower and slower variability (Fig. 2). An annual modulation of scintillation properties has been ob-

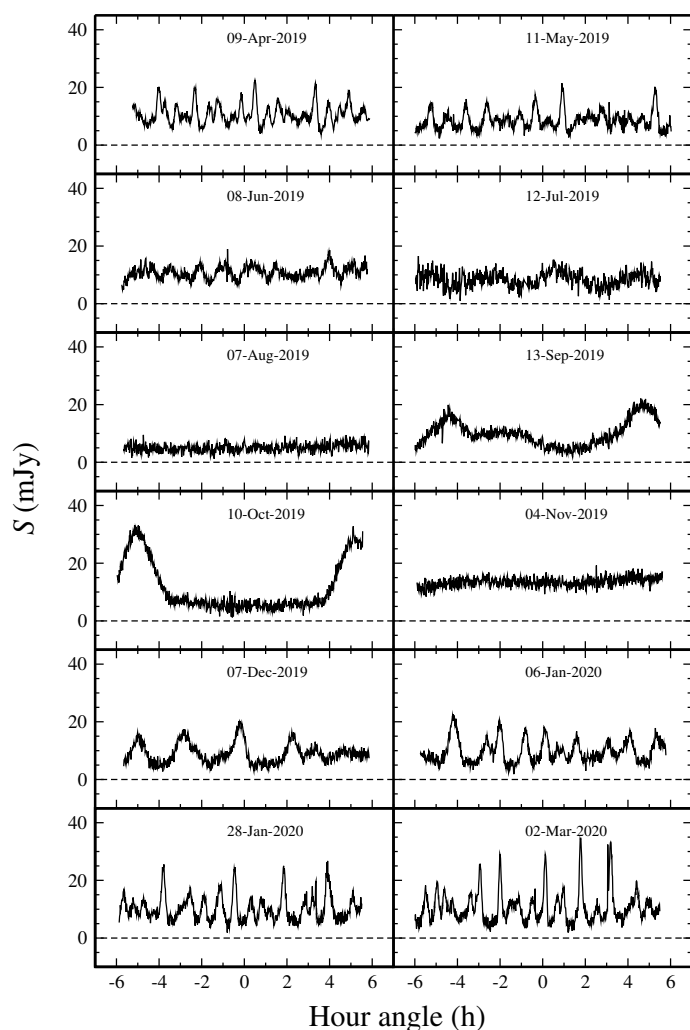


**Fig. 2.** Light curves of J1402+5347 observed over a year with a monthly cadence. The dates of the observations are indicated. The annual modulation in the rate of variations is apparent. We observe two standstills in August 2019 and November 2019, while the most rapid variations occurred in April 2019 and March 2020.

served in the other known intra-hour variables (Dennett-Thorpe & de Bruyn 2003; Walker et al. 2009; Bignall et al. 2019) and is caused by the annual change in the relative velocity of the Earth with respect to the plasma clouds due to the orbital motion of the Earth around the Sun. Motivated by this, we continued monitoring the source with a cadence of about one month. The intensity and the rate of the variations continued to fall, reaching a virtual ‘standstill’ in August. Following a brief period of slow variability in September and October, another standstill was observed in November. Post November, the rate and intensity of the variations have steadily increased, and by March 2020, they even exceeded the high levels seen in the discovery observation of April 2019.

## 3. Timescale analysis

The scintillation geometry and physical properties of the plasma clouds causing the scintillation can be determined from the annual variation of the timescale of the scintillations. We computed the scintillation timescale for each observation using two methods widely used in the analysis of time-series. The first method determines the decorrelation timescale from the noise-bias cor-

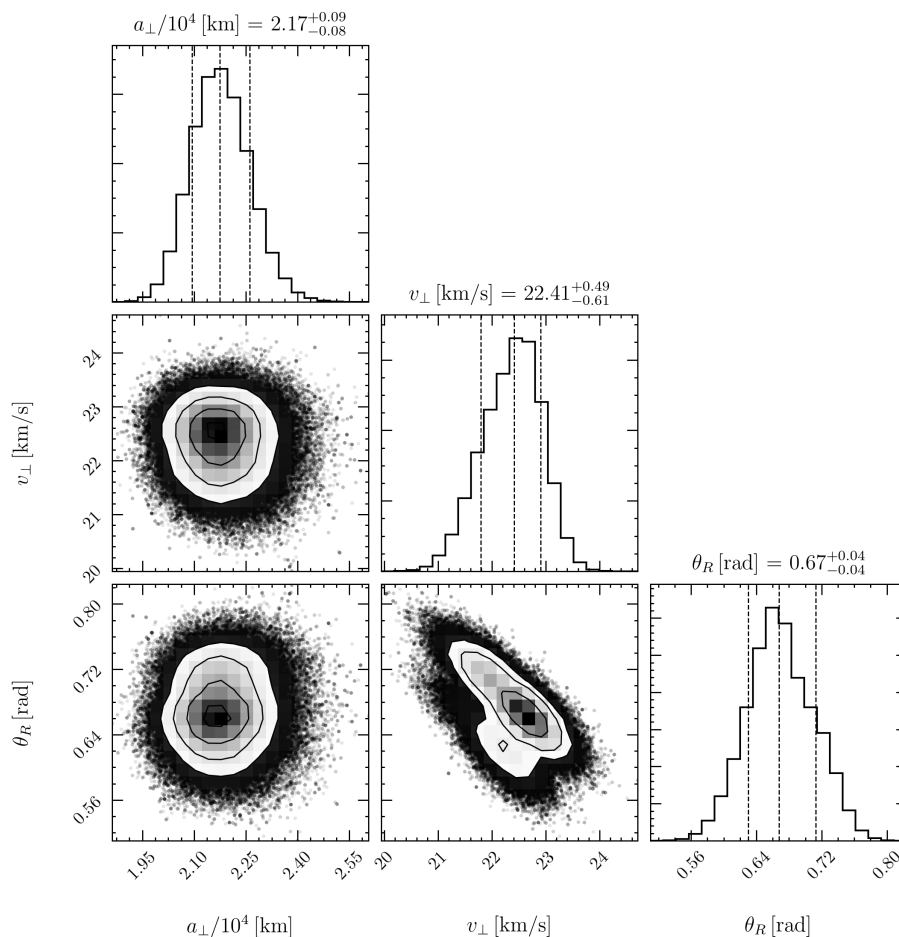


**Fig. 3.** Posterior distribution of model parameters describing the annual modulation of the scintillation rate. The panels on the diagonal are the marginalised one-dimensional posterior distributions. The dashed black lines are drawn at 0.16, 0.5, and 0.84 quartiles. The annotated text gives the best fit parameters and  $\pm 1\sigma$  bounds implied by the posterior distributions.

rected autocorrelation function directly computed from the light curves (Appendix B). The temporal lag at which the autocorrelation function of the variations falls below a specified threshold is taken as the timescale of the scintillations. For easy comparison with previous work (Dennett-Thorpe & de Bruyn 2003; Bignall et al. 2019), here we define the threshold as  $1/e$  times the peak value. This method is more accurate as it makes minimal assumptions. However, it is only effective for epochs of rapid variability as it requires several scintels to be observed within a single observation run (Dennett-Thorpe & de Bruyn 2003). For epochs near the standstills, we used a method commonly called Gaussian process regression (Appendix B). This method models the observed variations as a Gaussian process with a judiciously chosen functional form for the temporal covariance function. Although this method assumes an analytic form of the covariance function, it can effectively determine the decorrelation timescale and uncertainties even in epochs near the standstills (Bignall et al. 2019). The decorrelation timescales from both methods are tabulated in Table 1, and are in mutual agreement, within the errors, for all the epochs where both methods could be applied.

The scintillation timescale of just 6.5 min in March 2020 and the similarly short timescale in the April 2019 observations are remarkable. It represents the fastest interstellar scintillation reported to date, despite, compared to previous studies, the lower

frequency of observation where normally scintillations are expected to be significantly slower.

This timescale directly relates the physical size of the scintels to the transverse speed between the Earth and the scattering plasma. A single-epoch measurement cannot constrain the scintel size and the relative speed simultaneously. However the annual modulation in the scintillation timescale can be used to estimate both parameters. In particular, the two standstills critically constrain both the screen velocity and the geometry of the scintels. One annual standstill can be obtained when the screen velocity on the ecliptic plane equals the Earth’s orbital velocity. The second standstill requires the scintels to be anisotropic such that the standstill occurs when the relative velocity between the Earth and the plasma cloud is along the major axis of the scintels. We fit a simple model with one-dimensional scintels to the observed annual modulation, as suggested by (Walker et al. 2009; see Appendix C). The annual variation in this model is fully specified by three parameters: (a) the semi-minor axis of the scintels,  $a_{\perp}$ , (b) the systemic velocity of the scattering plasma along the minor axis of the scintels,  $v_{\perp}$ , and (c) the orientation of the major axis on the plane of the sky,  $\theta_R$  (measured from North to East). Figures 3 and 4 show the posterior distributions of the model parameters and the best-fitting annual-modulation curve respectively. We constrain the semi-minor axis of the scintels to be just  $a_{\perp} = 2.17(0.08) \times 10^4$  km. We note that the reduced

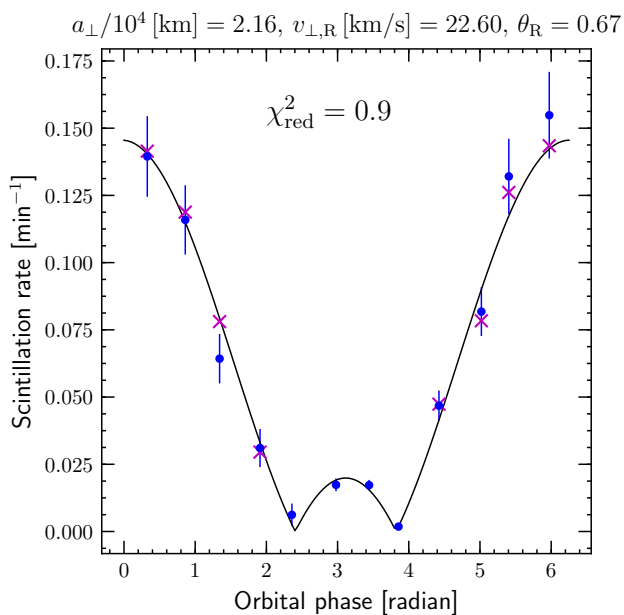


**Fig. 4.** Scintillation rate determined via Gaussian regression analysis (blue points with  $\pm 1\sigma$  errors) overplotted with the maximum likelihood model (black curve). The annotated text gives the model parameters and the reduced  $\chi^2$  of the fit. The phase at the vernal equinox is defined to be zero with phase increasing with time. Magenta crosses are the inverse of the scintillation timescale measured directly from the autocorrelation function of the light curves during epochs of sufficiently rapid variations.

chi-squared for the best-fitting model is close to unity which implies that the one-dimensional scintel model sufficiently and parsimoniously captures the annual variation in the data. To understand the degree of anisotropy implied by the data, we also computed the posterior distribution for a two-dimensional scintillation model (Appendix C). The two-dimensional model places a lower limit on the ratio of long and short axes of the scintels,  $R$ , of  $\log_{10}(R) > 2.12$ . As expected from the large anisotropy, the data do not constrain the space velocity of the scattering screen parallel to the long axis of the scintels.

#### 4. Discussion & Outlook

Incoherent synchrotron sources are generally expected to only display refractive interstellar scintillation. Refractive scintels of a point-like source will have a size equal to or larger than that of the first Fresnel zone:  $r_F = \sqrt{\lambda d / (2\pi)}$ , where  $\lambda$  is the wavelength and  $d$  is the distance to the scattering screen (Goodman & Narayan 2006). If the measured semi-minor axis of the scintels is associated with the Fresnel scale, the distance to the scattering plasma is  $d = 0.24$  pc which is within the Sun’s sphere of gravitational influence. This would place the scattering plasma within the canonically defined Oort cloud.

If J1402+5347 is unusually compact, then it may display diffractive interstellar scintillations as is usually seen in pulsars. In this case, the scintel size is associated with the diffractive scale. Because the diffractive scale can be much smaller than the Fresnel scale, the data admits significantly larger screen distances in the diffractive regime. Regardless, the length-scale of scintels cannot be smaller than the projected size of the source at the scattering screen. We consider, for simplicity, a circular source of angular radius  $\theta_{\text{src}}$ . The requirement  $d\theta_{\text{src}} < a_{\perp}$  places a constraint on the apparent brightness temperature of the source of  $T_b > 10^{11}(d/\text{pc})^2$  K.

Walker et al. (2017) have shown a statistical astrometric association between sight lines to sources showing intra-hour variability and hot stars such as Vega, Spica, and Alhakim. They also find that the long-axis of the scintels of IHV’s preferentially point towards the associated star. We searched the Hipparcos catalogue to see if the sight-line to J1402+5347 passes anomalously close to any known O, B or A-type star (see Fig. 5). We find that the B3 star Alkaid ( $\eta$  UMa, HIP 67301) at a distance of  $d = 32$  pc is unusually close to the sightline towards J1402+5347. The volume density of B-type stars in the Hipparcos catalogue that lie within a 50 degree wide cone around this sight-line is about  $4.3 \times 10^{-5}$  pc<sup>-3</sup>. The impact parameter of the sight-line with Alkaid is about 2.7 pc and the angle between the scintel long-axis and the star-ward direction in case of J1402+5347- Alkaid pairing is about  $9 \pm 3$  deg. The odds of finding a B-type star by chance with the observed impact parameter or closer, and with the observed angular alignment or better is about 0.2%. In addition, the space velocity components of Alkaid with respect to the Solar system’s barycentre are  $-17.8$  km s<sup>-1</sup> and  $-2.2$  km s<sup>-1</sup> along the RA and DEC axes respectively. This is about 9 km s<sup>-1</sup> different from the space velocity component of the scattering plasma as constrained by our observations, although, as pointed out by Walker et al. (2017), a clear agreement between space velocities may be precluded due to free expansion of the scattering plasma, and to a lesser extent, by projection effects. Regardless, an association of the scattering plasma with Alkaid sets  $d = 32$  pc and puts a rather extreme lower limit to the apparent brightness temperature of J1402+5347 of  $T_b > 10^{14}$  K. This limit can be slightly ameliorated if we postulate that the radio source itself is extended precisely along the major axis of the scintels.

An association with Alkaid also has critical implications for the variance in the scattering properties of the Galactic plasma at large. The angular broadening expected from the line-of-sight integrated Galactic plasma (unrelated to the scattering screen discussed here) is estimated to be about 0.36 mas by the widely used NE2001 model (Cordes & Lazio 2002). The brightness temperature necessary for an association with Alkaid however requires a source diameter to not exceed about 8.6  $\mu$ as, which is 40 times smaller than the anticipated angular broadening. An association with Alkaid therefore suggest that the bulk of the scattering in the Galactic ISM must happen in highly localised clumps so that such a large sight-line to sight-line variation can be accounted for.

Whether the scattering plasma is located in the Oort cloud or is associated with Alkaid, may be determined via by extending the theoretical analysis like the one of Goodman & Narayan (2006) to the case of highly anisotropic scintels, and by broadband observations of J1402+5347 at higher frequencies. If the observed scattering at 1.4 GHz is indeed diffractive, two effects must be seen in such observations: (a) the scintillations will decorrelate on frequency scales  $\Delta\nu/\nu \ll 1$ , and (b) the transition to weak scattering must happen at frequencies several times larger than 1.4 GHz and similarly large light-curve variations must then extend to such high frequencies. If the scattering is associated with the Oort cloud, then the observed variations are due to refractive scintillations in the weak scattering regime. We therefore expect to observe broadband variations ( $\Delta\nu/\nu \sim 1$ ) at higher frequencies with a continuously declining level of fractional variations with increasing frequency. The observations of 09-Apr-2019 show that the variations in the upper and lower end of the  $\Delta\nu/\nu \approx 15\%$  observing band are very similar, with a Pearson correlation coefficient of 0.84 (Appendix D), suggesting refractive variations and that the scattering plasma is located in the Oort cloud. However, further theoretical investigation on the spectral

decorrelation properties of highly anisotropic scintels are necessary to make a definitive determination of the distance to the scattering screen.

We end by noting that due to the larger apparent source sizes at lower frequencies, fast intra-hour variability at decimetre wavelengths will be significantly biased towards intervening plasma clouds that are nearby. The discovery of rapid scintillation in J1402+5347 in early Apertif data bodes well for ongoing wide-field surveys in the decimetre band. Based on the discovery of J1402+5347 and the sky area covered by the Apertif survey at the time, we expect to discover roughly ten more of such systems and indeed several new IHV sources have more recently been identified in Apertif data (Oosterloo et al. in prep).

## References

- Bignall, H., Reynolds, C., Stevens, J., et al. 2019, MNRAS, 487, 4372  
 Bignall, H. E., Jauncey, D. L., Lovell, J. E. J., et al. 2003, ApJ, 585, 653  
 Bignall, H. E., Jauncey, D. L., Lovell, J. E. J., et al. 2007, Astronomical and Astrophysical Transactions, 26, 567  
 Cordes, J. M. & Lazio, T. J. W. 2002, arXiv e-prints, astro  
 Cutri, R. M., Wright, E. L., Conrow, T., et al. 2012, Explanatory Supplement to the WISE All-Sky Data Release Products, Explanatory Supplement to the WISE All-Sky Data Release Products  
 de Bruyn, A. G. & Macquart, J. P. 2015, A&A, 574, A125  
 Dennett-Thorpe, J. & de Bruyn, A. G. 2003, A&A, 404, 113  
 Foreman-Mackey, D., Agol, E., Ambikasaran, S., & Angus, R. 2017, AJ, 154, 220  
 Foreman-Mackey, D., Hogg, D. W., Lang, D., & Goodman, J. 2013, PASP, 125, 306  
 Goldreich, P. & Sridhar, S. 2006, ApJ, 640, L159  
 Goodman, J. & Narayan, R. 2006, ApJ, 636, 510  
 Jarrett, T. H., Cluver, M. E., Magoulas, C., et al. 2017, ApJ, 836, 182  
 Pen, U.-L. & King, L. 2012, MNRAS, 421, L132  
 Pen, U.-L. & Levin, Y. 2014, MNRAS, 442, 3338  
 Walker, M. A., de Bruyn, A. G., & Bignall, H. E. 2009, MNRAS, 397, 447  
 Walker, M. A., Tuntsov, A. V., Bignall, H., et al. 2017, ApJ, 843, 15

*Acknowledgements.* We dedicate this paper to the memory of Ger de Bruyn and of J.P. Macquart. HKV thanks Mark Walker for discussions. Credit is also due to Mark Walker for pointing out the possible association with Alkaid. EAKA is supported by the WISE research programme, which is financed by the Netherlands Organisation for Scientific Research (NWO). YM acknowledges funding from the European Research Council under the European Union's Seventh Framework Programme (FP/2007-2013)/ERC Grant Agreement No. 617199. LCO acknowledges funding from the European Research Council under the European Union's Seventh Framework Programme (FP/2007-2013)/ERC Grant Agreement No. 617199. JMvdH acknowledges funding from the European Research Council under the European Union's Seventh Framework Programme (FP/2007-2013)/ERC Grant Agreement No. 291531 ('HISToryNU'), JvL acknowledges funding from the European Research Council under the European Union's Seventh Framework Programme (FP/2007-2013) / ERC Grant Agreement No. 617199 ('ALERT'), and from Vici research programme 'ARGO' with project number 639.043.815, financed by the Netherlands Organisation for Scientific Research (NWO). This work makes use of data from the Apertif system installed at the Westerbork Synthesis Radio Telescope owned by ASTRON. ASTRON, the Netherlands Institute for Radio Astronomy, is an institute of the Dutch Science Organisation (De Nederlandse Organisatie voor Wetenschappelijk Onderzoek, NWO).

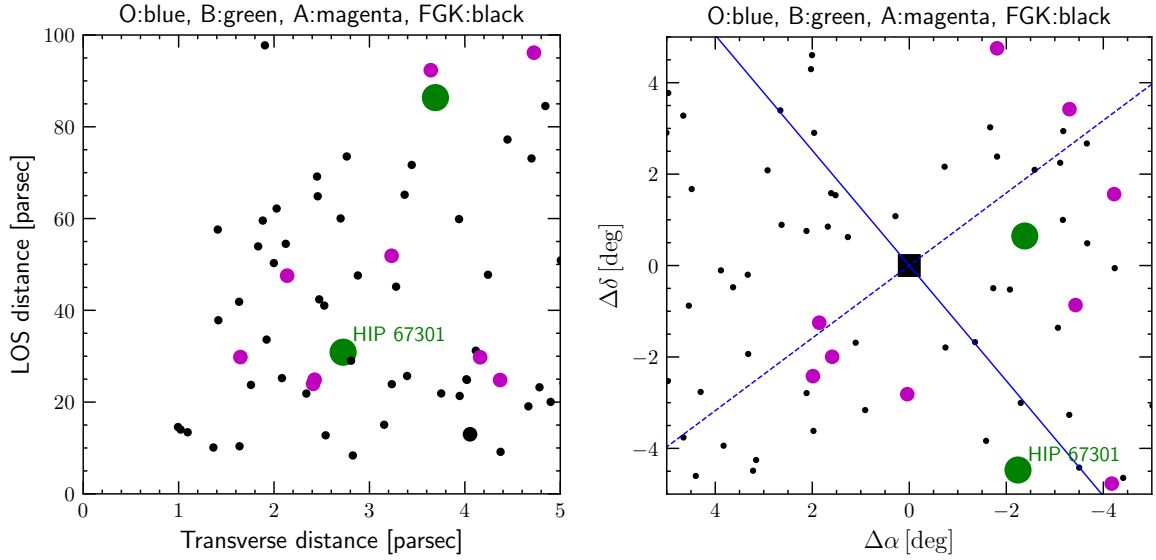


**Fig. 5.** Left panel: Line of sight and transverse distance of stars in the *Hipparcos* catalogue with respect to the sight-line towards J1402+5347. The stars are colour-coded by their spectral type (legend in annotated text). Right panel: same as left panel but with the stars plotted in the plane of the sky. The central black square is J1402+5347. The solid and dashed blue lines mark the orientation of the major and minor axes of the scintells respectively.

**Table 1.** Annual modulation statistics: Noise bias (determined from the variance of flux density variation between adjacent points in the light curve) has been subtracted from the modulation index. The ACF and GP refer to estimates from direct numerical computation of the autocorrelation function and the Gaussian process analysis respectively. The errors on the GP scintillation rate estimates do not include the 10% uncertainty on the scintillation rate due to uncertainty in the kernel parameters (to be added in quadrature). Although scintillation rates were used in the annual modulation fits, we also quote the timescales here for easy comparison to previous work. ND indicates that not enough scintells are observed for robust timescale estimation.  $1-\sigma$  uncertainties are given in the parentheses. In case of significantly asymmetric errors, the  $1-\sigma$  upper and lower bounds are given in the super-scripted and sub-scripted text respectively.

Date	modulation index	ACF timescale [min]	GP timescale [min]	GP scintillation rate [ $\text{min}^{-1}$ ]
09-Apr-2019	0.31	7.1(0.7)	7.2(0.8)	0.140(0.006)
11-May-2019	0.34	8.4(0.9)	8.6(1.0)	0.116(0.006)
08-Jun-2019	0.17	13(2)	16(2)	0.064(0.007)
12-Jul-2019	0.22	34(8)	32(7)	0.031(0.006)
07-Aug-2019	0.15	ND	$161^{+149}_{-64}$	0.006(0.004)
13-Sep-2019	0.42	ND	$57.7^{+5.5}_{-5}$	0.017(0.002)
10-Oct-2019	0.75	ND	$58^{+3}_{-3}$	0.017(0.001)
04-Nov-2019	0.07	ND	$546^{+241}_{-193}$	0.002(0.001)
07-Dec-2019	0.37	21(4)	21(2)	0.047(0.003)
06-Jan-2020	0.39	13(2)	12(1)	0.082(0.004)
28-Jan-2020	0.40	7.9(0.9)	7.6(0.8)	0.132(0.005)
02-Mar-2020	0.50	7(0.7)	6.5(0.7)	0.155(0.005)

## Appendix A: Interferometric data reduction.

The observations of J1402+5347 presented here were performed with the Apertif phased-array feed system, recently installed on the WSRT. With Apertif, 40 partially overlapping beams, each having a FWHM of about 35 arcminutes, are formed on the sky. The data from each beam are being used independently to image, using standard aperture synthesis, the region covered by each beam. The total area imaged by combining the images from all beams is about  $2:5 \times 2:5$  with a spatial resolution of  $12'' \times 17''$  at the declination of J1402+5347. The observing band was 122 MHz wide, divided in 156 channels, centred on 1.365 GHz. J1402+5347 was detected in three overlapping beams. Each observation had a duration of 11 to 11.5 hours. The calibration of the data from each beam followed standard procedures, involving RFI excision, flux-, bandpass- and cross-calibration using 3C147, followed by self-calibration. The resulting images suffered from small direction-dependent imaging errors, which were corrected for by using standard peeling techniques. This in particular applies to the strong source 3C295, located  $2:0$  SW of J1402+5347, which, because of the large distance from the beam centres, suffered from large direction-dependent effects. The resulting images are noise limited with a noise level of about  $30 \mu\text{Jy beam}^{-1}$ , varying slightly between observations.

To construct the light curves, the source model resulting from the self-calibration was subtracted from the visibilities, except for the source model for J1402+5347, giving a visibility data set containing only emission from J1402+5347. The phase centre of this visibility data set was shifted to the position of J1402+5347 so that the phases of all visibilities are zero. Finally, for each time stamp, the visibilities of all baselines and frequencies were summed to obtain the flux density of J1402+5347 for each time stamp, giving, after primary beam correction, the light curves shown in Fig. 2.

To check the accuracy of the light curves, the same procedure was followed for J1403+5349, a source of very similar flux density, 9 arcminutes W of J1402+5347. An example of such a comparison is shown in Fig. A.1.

## Appendix B: Determination of scintillation timescale.

We computed the scintillation timescale using both the autocorrelation function (ACF) and Gaussian process modelling (GP).

- *Autocorrelation function*: We follow a procedure which closely mimics that presented by Bignall et al. (2003). We first subtract the mean flux density from the light curves to obtain a time series,  $x_i$  with sampling interval  $\Delta t$ . For each pair  $ij$  we compute the product  $x_i x_j$ . The list of products is then binned on a grid of size  $\Delta t$ , and all products falling into the same bin are averaged. Thermal noise only biases the zeroth bin as it is uncorrelated between light curve samples. This bias, equal to the variance of the noise, is estimated to be equal to half the variance of the difference between successive samples in the time series. The  $1/e$  timescale,  $t_e$ , is estimated using a straight-line fit to a segment of the autocorrelation function containing five samples, centred on the sample that is closest to  $1/e$ . The error on the scintillation timescale is given by  $\sigma_{t_e} = \epsilon t_e / \sqrt{N}$ , where  $N$  is the number of observed cycles of variation on timescale  $t_e$  and  $\epsilon$  is a factor or order unity that depends on the exact profile of the autocorrelation function around  $t_e$ . If the total duration of observation is  $T$  ( $\sim 11.5$  hr in our case), then  $N = (T/t_e)$ .

The factor  $\epsilon$  has been estimated via numerical Monte Carlo techniques (Dennett-Thorpe & de Bruyn 2003; Bignall et al. 2003) to be in the range 0.25 to 0.9. Here, we conservatively assume  $\epsilon = 1$ . The timescale and its errors thus computed are only accurate when several scintells are observed which is not the case during the standstills. An example autocorrelation function is plotted in Fig. B.1.

- *Gaussian process*: The temporal scintillation is modelled as a Gaussian process with a covariance function given by a damped exponential:  $K(\Delta t) = K_0 \exp(c\Delta t) \cos(d\Delta t)$ , where  $\Delta t$  is the temporal lag and  $K_0$ ,  $c$  and  $d$  are model parameters (Bignall et al. 2019). This choice for the covariance function is motivated by the shape of the autocorrelation function that shows a steep roll-off at small lags, follows by oscillatory behaviour due to the dominant spectral mode in the light curves (see Fig. B.3) We assume that the scintillation is a stationary process, which means that the parameters remain the same over different epochs and the variation in the timescale of scintillation can be modelled by a single epoch-dependent scale factor,  $k$ , via the substitution  $\Delta t \rightarrow k\Delta t$ . This allows us to estimate the scintillation timescale and the associated uncertainty even for epochs close to the standstill by employing our knowledge of the co-variance function from epochs of rapid variability. We determined the parameters ( $K_0$ ,  $c$ , and  $d$ ) from the April 2019 light curve alone instead of using a fit using the entire annual data-set (Bignall et al. 2019). With these parameter values fixed, we determined the temporal scale factor  $k$  for each epoch with a single-parameter Gaussian regression.

All data were mean subtracted prior to regression analysis and a noise variance term (estimated from time differences) was added to the diagonal elements of the covariance matrix. For the April 2019 dataset, we fixed  $K_0$  to equal the total variance in the scintillations:  $K_0 = 3.477105 \text{ mJy}^2$ , and estimated  $c$  and  $d$ . The best-fit estimates were  $\log(c) = -3.80 \pm 0.10$  and  $\log(d) = -1.86 \pm 0.05$ . The posterior distributions for these parameters were computed using the emcee software (Foreman-Mackey et al. 2013) and are plotted in Fig. B.2. The numerically computed auto-correlation function and the best-fit kernel are plotted together for comparison in Fig. B.3.

Next, we held  $K_0$ ,  $c$  and  $d$  fixed at the best-fit values quoted above and used the `celerite` (Foreman-Mackey et al. 2017) package to fit a single scale parameter  $k$ . The  $1/e$  crossing timescale for the April 2019 epoch is largely set by the value of parameter  $c$ , which is determined with a formal error of about 10%. To account for this uncertainty in our error budget, we added a 10% error in quadrature to the formal errors on the timescale from the Gaussian process regression analysis.

Throughout our analysis, the likelihood computations were done using routines from the `celerite` package (Foreman-Mackey et al. 2017), the best-fit values were determined using `scipy.optimize` with the L-BFGS-B method, and the posterior distributions were sampled using the `emcee` package (Foreman-Mackey et al. 2013).

## Appendix C: Annual modulation.

The timescale of temporal scintillation due to anisotropic scattering is given by (Walker et al. 2009)

$$t_s = \frac{R a_{\perp}}{\sqrt{v_{\parallel \text{rel}}^2 + R^2 v_{\perp \text{rel}}^2}} \quad (\text{C.1})$$

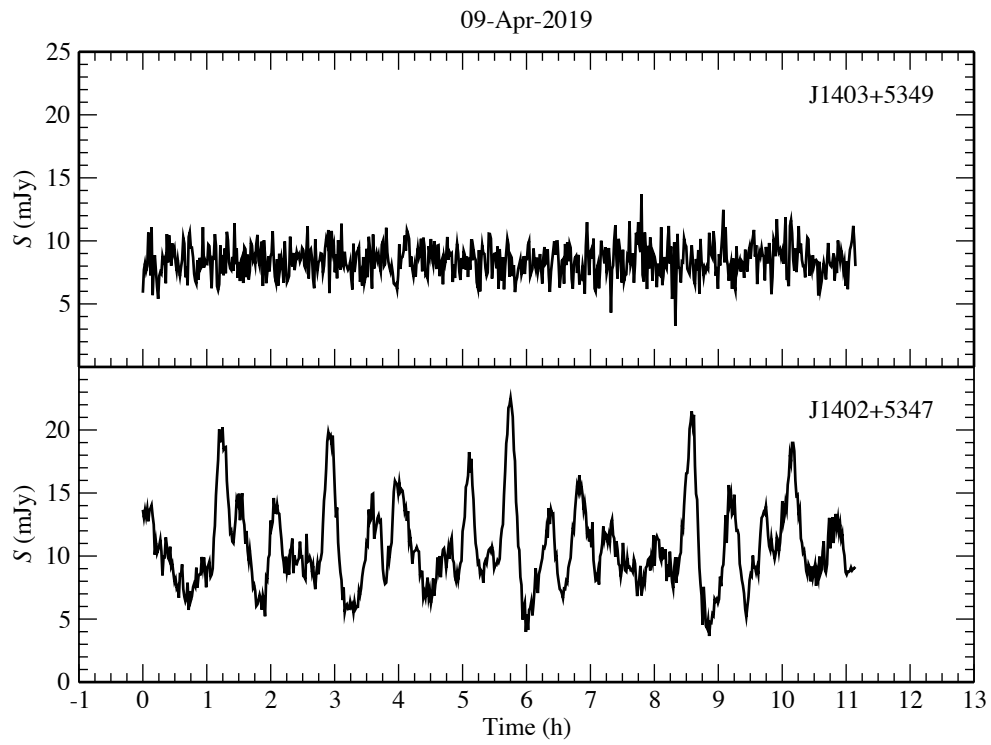


**Fig. A.1.** Light curves derived for April 9, 2019, of the variable source J1402+5347 and a steady comparison source J1403+5349, 9 arcminutes west of J1402+5347, illustrating the accuracy of the method for constructing the light curves. The horizontal axis is time since the start of the observation.

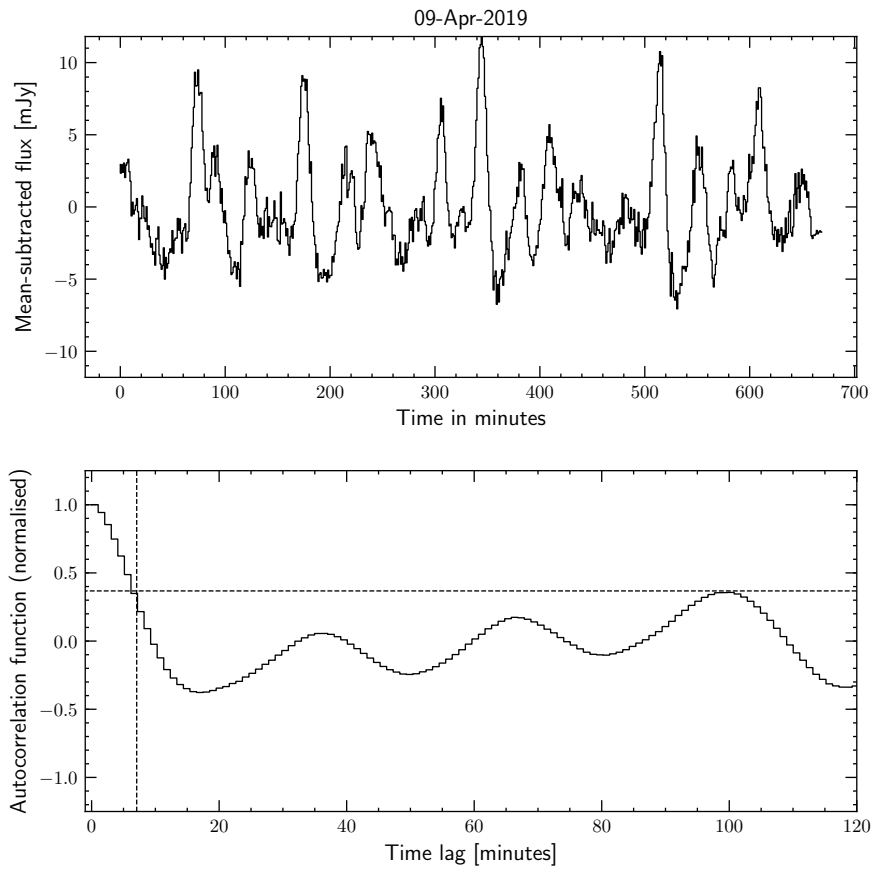


**Fig. B.1.** Numerical ACF computation: Mean subtracted light curve (top-panel) and the autocorrelation function (bottom panel) for the April 9, 2019 light curve.

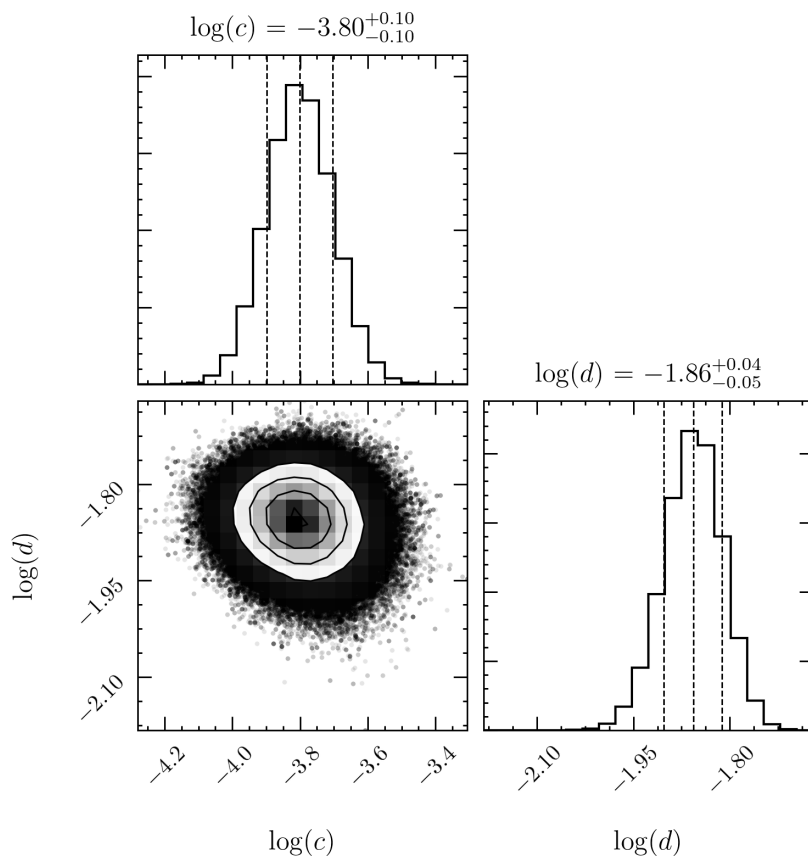


**Fig. B.2.** Gaussian process kernel parameters: Posterior distribution of Gaussian process kernel parameters for the April 9, 2019 data-set. The total variance.  $K_0$  was fixed to equal the noise-bias corrected variance of the light curve and only the scale parameters  $c$  and  $d$  were estimated. The dashed lines are placed at the 16, 50, and 84<sup>th</sup> quantiles of the marginalised 1-D distributions. The fractional error in the estimation of parameter  $c$  is about 10%.

where  $R = a_{\parallel}/a_{\perp}$  is the anisotropy of the scintels,  $a_{\perp}$  and  $a_{\parallel}$  are the length-scale of scintels along the minor and major axes respectively,  $v_{\perp, \text{rel}}$  and  $v_{\parallel, \text{rel}}$  are the relative velocity between the Earth and the scintels along the minor and major axes of the scintels respectively. For highly anisotropic scintels (Walker et al. 2009), we can set  $R \rightarrow \infty$  and get  $t_s = a_{\perp}/v_{\perp, \text{rel}}$ . The annual modulation profile can be fit with a three parameter model. The parameters are (i) the semi-minor axis of the scintels,  $a_{\perp}$ , (ii) the orientation of the major axis of the scintels in the plane of the sky,  $\theta_R \in (0, 2\pi]$ , measured from North towards East, and (iii) the screen velocity in the plane of the sky perpendicular to the major axis of the scintels  $v_{\perp} \geq 0$  (defined to be along  $\theta_R - \pi/2$ ). We carry out our fits in a tangent plane perpendicular to the sight-line with cardinal axes along the directions of increasing RA ( $\hat{\alpha}$ ) and DEC ( $\hat{\delta}$ ). If  $\mathbf{v}_{\oplus}(t) = \hat{\alpha}v_{\oplus}^{\alpha} + \hat{\delta}v_{\oplus}^{\delta}$  is velocity of the Earth projected onto this plane, then the relative velocity perpendicular to the major axis of scintels is given by  $v_{\perp, \text{rel}} = |v_{\perp} - v_{\oplus}^{\delta} \sin \theta_R + v_{\oplus}^{\alpha} \cos \theta_R|$ . We fit the above equation to the scintillation timescales tabulated in Table 1 (column ‘‘GP scintillation rate’’). We carried out the fits to the scintillation rate instead of the scintillation timescale to avoid infinities in the model. First, we carried out a brute-force search for the maximum likelihood value on a coarse three-dimensional parameter grid spanned by  $10^8 \text{ cm} < a_{\perp} < 5 \times 10^{10} \text{ cm}$ ,  $0 \text{ km s}^{-1} < v_{\perp} < 100 \text{ km s}^{-1}$ , and  $0 < \theta_R < 2\pi$ . The likelihood had its peak value around  $a_{\perp} \approx 2 \times 10^9 \text{ cm}$ ,  $v_{\perp} \approx 22 \text{ km s}^{-1}$  and  $\theta_R \approx 0.7$ . We then used the emcee software (Foreman-Mackey

et al. 2013) to obtain the final fit values and their formal errors. We used 200 randomly initialised walkers, each walking 2000 steps. We imposed a flat prior on the parameters in the range  $2 \times 10^8 \text{ cm} < a_{\perp} < 2 \times 10^{10} \text{ cm}$ ,  $15 \text{ km s}^{-1} < v_{\perp, R} < 35 \text{ km s}^{-1}$ , and  $0.1 < \theta_R < 1.1$ . The posterior parameter distributions were computed and plotted from the emcee samples using the corner package.

We also ran a separate MCMC simulation to sample the posterior distribution for a two-dimensional scintillation model given in equation C.1. The additional parameters in the two dimensional model and  $R$ . We placed the prior bounds  $v_{\parallel} \in [0, 100) \text{ km/s}$  and  $\log_{10} R \in [0, 4)$ , with the relative velocity parallel to the scintel long axis given by  $v_{\parallel, \text{rel}} = |v_{\parallel} - v_{\oplus}^{\delta} \cos \theta_R - v_{\oplus}^{\alpha} \sin \theta_R|$ . The posterior distributions are given in Fig. C.1.

## Appendix D: Broad-band nature of scintels

To investigate the presence of a possible frequency dependence of the intensity fluctuations, we constructed separate light curves for the upper and the lower halves of the observing band for the observations of April 9, 2019. These separate light curves are shown in Fig. D.1 where the blue line is the light curve for the frequency range 1311 – 1408 MHz and the red line for the range 1408 – 1505 MHz. It is clear from this figure that the light curves are very similar showing that there is no frequency structure with

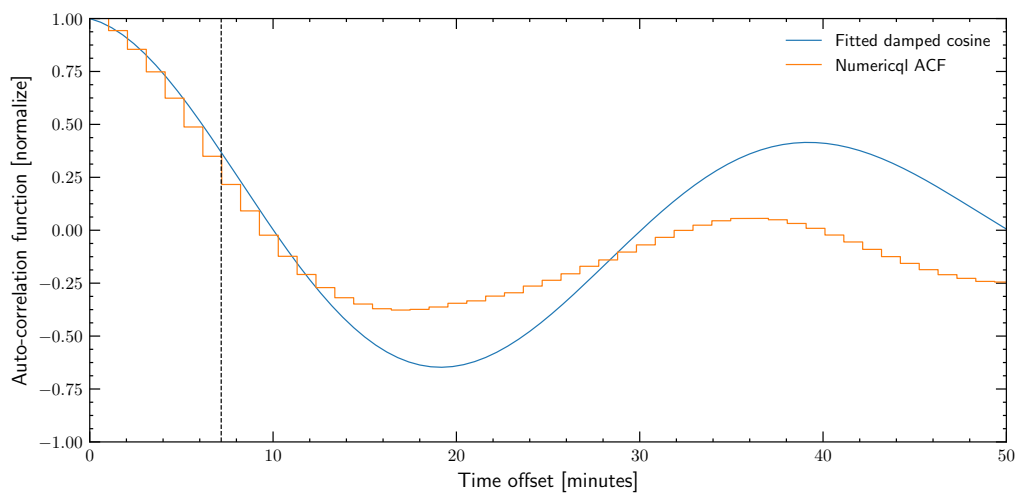


**Fig. B.3.** Best fitting kernel: Numerically computed ACF over-plotted with the best-fit Gaussian kernel for the April 9, 2019, light curve. The decorrelation timescale of the Gaussian kernel is indicated with the dashed black line. The quasi-sinusoidal oscillations at large delay are not ideally captured by the analytic form of the kernel. However, the decay to the  $1/e$ -value at small delays is well captured and is the most relevant to the estimation of scintillation rates.

the observing band. The Pearson correlation coefficient between the two light curves is 0.84.

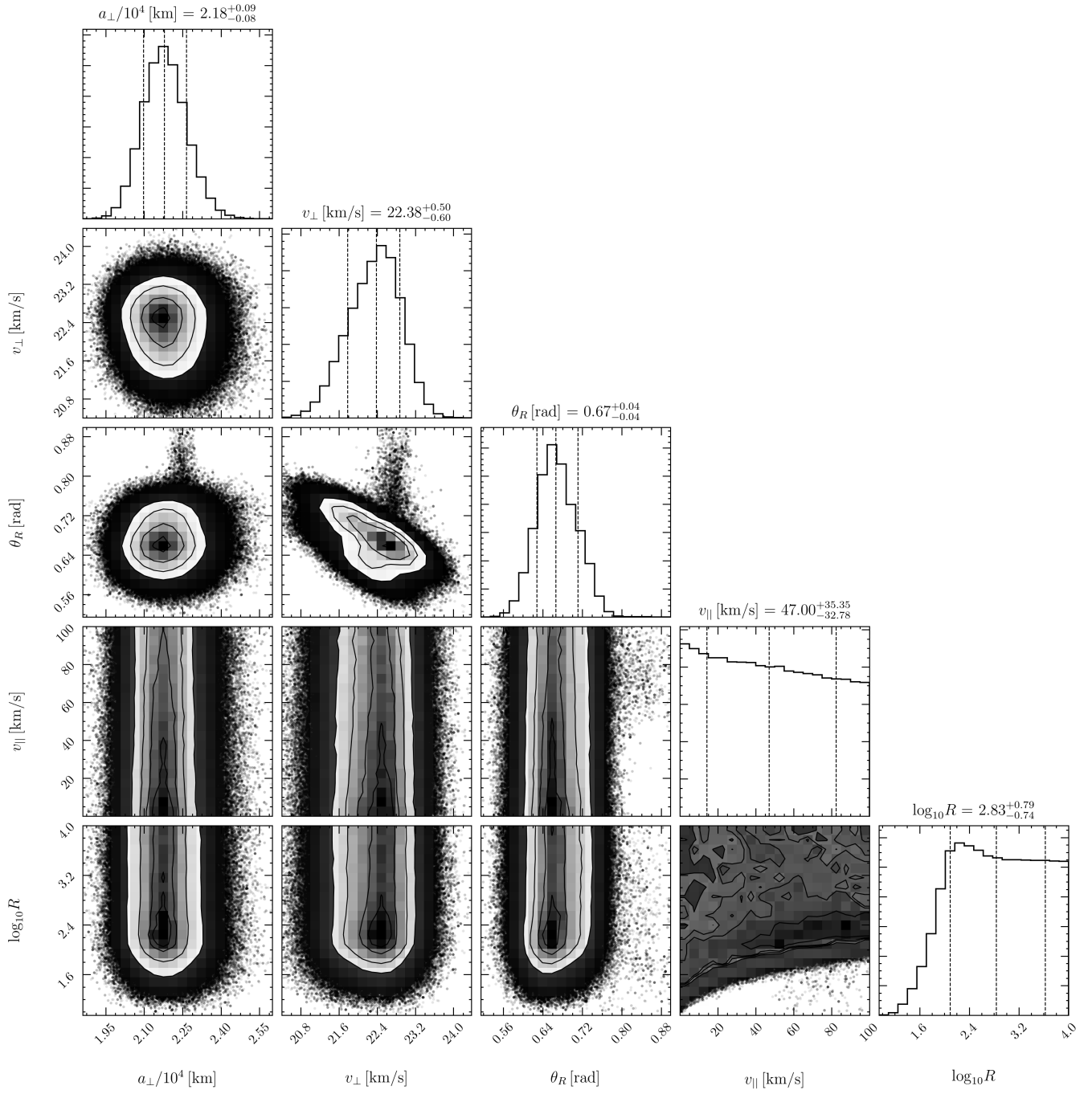


**Fig. C.1.** Same as Fig. 3, but for a two dimensional scintel model given in equation C.1.

Apertif IHV 1 09-Apr-2019

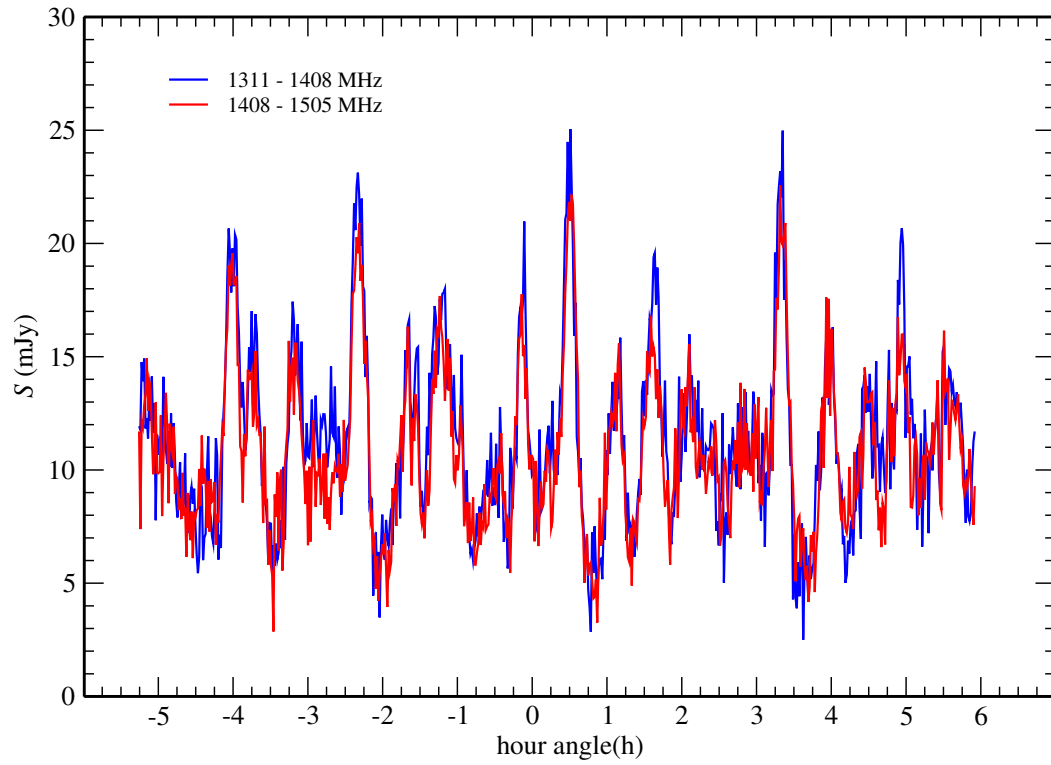


**Fig. D.1.** Separate light curves for the lower- and the upper halves of the observing band of the discovery observation of April 9, 2019. The blue line is the light curve for the frequency range 1311 – 1408 MHz and the red line for the range 1408 – 1505 MHz.